INL/JOU-24-81998-Revision-0

Wrought FeCrAl alloy (C26M) cladding behavior and burst under simulated loss-of-coolant accident conditions

January 2025

Ryan Terrence Sweet, Caleb Massey, Jacob Aaron Hirschhorn, Samuel Bell, Kenneth Kane

Changing the World's Energy Future

INL is a U.S. Department of Energy National Laboratory operated by Battelle Energy Alliance, LLC

INL/JOU-24-81998-Revision-0

Wrought FeCrAl alloy (C26M) cladding behavior and burst under simulated loss-of-coolant accident conditions

Ryan Terrence Sweet, Caleb Massey, Jacob Aaron Hirschhorn, Samuel Bell, Kenneth Kane

January 2025

Idaho National Laboratory
Idaho Falls, Idaho 83415

http://www.inl.gov

Prepared for the
U.S. Department of Energy
Under DOE Idaho Operations Office
Contract DE-AC07-05ID14517

Wrought FeCrAl Alloy (C26M) Cladding Behavior and Burst under Simulated Loss-of-Coolant Accident Conditions

R.T. Sweet[a,*], C.P. Massey[b], J.A. Hirschhorn[a], S.B. Bell[b], K.A. Kane[b]

[a] *Idaho National Laboratory, 1955 Fremont Ave, Idaho Falls, 83415, ID, USA*
[b] *Oak Ridge National Laboratory, 1 Bethel Valley Rd, Oak Ridge, 37830, TN, USA*

Abstract

Cladding burst experiments for FeCrAl cladding were performed in the Severe Accident Test Station facility at Oak Ridge National Laboratory. These experiments were simulated using the BISON fuel performance code to better understand the cladding plastic behavior and failure under simulated loss-of-coolant accident conditions. 3D cladding surface boundary conditions were generated using composite axial and azimuthal profiles from experiment thermocouple data. To improve the simulation analysis capabilities in BISON for cladding burst behavior, new thermal creep, plasticity, and failure stress models specific to C26M, a wrought FeCrAl alloy, were developed and implemented.

Initial cladding burst results indicated a general underprediction in the failure temperature of the six cladding burst simulations versus the observed failure temperatures. Close investigation of the experiment timing versus the underlying tensile test data revealed that, compared with the tensile specimens, the cladding tubes did not experience the same long holding time at high temperatures. New tensile tests were performed at high temperatures using a temperature ramp similar to the simulated loss-of-coolant accident experiments. These new tensile curves showed an approximately 80% increase in the ultimate tensile strength of the C26M alloy, indicating that a holding time of 10 minutes at 700°C and 800°C allows annealing to change the material microstructure.

Using the updated tensile properties, the burst temperatures and stresses from the simulations showed remarkable agreement with the experimental results. This study was then extended by varying the initial pressure to highlight the burst temperature difference between standard Zircaloy-4 and C26M cladding under equivalent conditions. The results show that C26M has a burst temperature that is approximately 70–130 K greater than that of Zircaloy-4.

These modeling predictions can be further improved by collecting high-temperature tensile data for C26M beyond the temperature ranges used in this work.

Keywords: Fuel Performance, FeCrAl Cladding, Cladding Burst, Loss-of-Coolant Accident, BISON

1. Introduction

After the 2011 Tōhoku earthquake and the subsequent accident at the Fukushima Daiichi Nuclear Generating Station—the first large-scale nuclear accident since the 1980s—the US Department of Energy

*Corresponding author
Email address: ryan.sweet@inl.gov (R.T. Sweet)

This manuscript has been authored by Battelle Energy Alliance, LLC, under Contract No. DE-AC07-05ID14517, and UT-Battelle, LLC, under contract DE-AC05-00OR22725, with the US Department of Energy (DOE). The US government retains and the publisher, by accepting the article for publication, acknowledges that the US government retains a nonexclusive, paid-up, irrevocable, worldwide license to publish or reproduce the published form of this manuscript, or allow others to do so, for US government purposes. DOE will provide public access to these results of federally sponsored research in accordance with the DOE Public Access Plan (https://www.energy.gov/doe-public-access-plan).

began the Fuel Cycle Research and Development Advanced Fuels Campaign. This research and development program was designed to identify fuel–cladding systems that perform better under accident conditions than incumbent zirconium-based alloys [1] and to develop these systems to commercial viability. The primary goal for these fuel systems was to reduce (through a replacement alloy or coating) the hydrogen generation rate of the core materials in high-temperature steam. Other improvements identified for these alloys included enhanced fission product retention, structural integrity in high-temperature steam, and reduced fuel–cladding chemical and mechanical interaction. This effort ultimately led to the identification, testing, and development of the iron-chromium-aluminum (FeCrAl) alloy cladding material.

To increase the safety margin of light-water reactor fuel in severe accident scenarios, alternative cladding materials have been proposed [2]. Particular focus has been given to a lower chromium-content class of FeCrAl alloys because, compared with zirconium-based alloys, these alloys exhibit significantly slower oxidation kinetics in high-temperature steam [3]. Previous studies have shown that in high-temperature steam, FeCrAl cladding oxidizes approximately 100× slower than zirconium-based alloys and type-304 stainless steels. Increased oxidation resistance may allow for more time to mitigate further damage that could result from an accident. Previous core-resolved studies have shown additional coping time in short-term station blackout conditions owing to the enhanced oxidation resistance of FeCrAl cladding [4, 5]. Specifically, these studies demonstrated that, in an unmitigated station blackout scenario, using FeCrAl as a cladding replacement can increase the coping time by up to 4.5 h.

Compared with zirconium-based alloys, FeCrAl alloys also possess superior mechanical strength, which allows for the option to change the cladding thickness to achieve similar mechanical integrity. Because of its strength, stainless-steel cladding has been suggested to exhibit better resistance to pellet–clad mechanical interaction failure than zirconium-based alloys [6]. However, the thermal and irradiation creep rates of FeCrAl are orders of magnitude slower than that of Zircaloy under equivalent conditions, changing the expected fuel rod gap closure behavior and the cladding response under pellet–clad mechanical interaction failure [7].

Replacing zirconium-based alloy fuel cladding with FeCrAl alloy fuel cladding does change the neutronics in the core. These FeCrAl alloys have thermal neutron cross sections that are approximately 12–16× larger than those of zirconium-based alloys. This decreases the reactivity of the core and subsequently decreases the potential cycle length for operation [8]. To counteract this decrease in reactivity, increased fuel enrichment or increased fuel mass have been considered. Alternatively, because of the higher strength of FeCrAl, decreasing the cladding thickness to reduce the neutronic penalty from using the alloy is also possible. To achieve an equivalent cycle length, the cladding thickness would either have to be nearly half of the expected thickness for Zircaloy, or the fuel enrichment would have to be increased past 5%. This presents a challenge because many fuel fabrication facilities and reactors are currently licensed for a maximum enrichment of 5% [9]; however, renewed efforts are underway to increase this limit [10], thereby allowing a greater range of options to potentially realize new accident-tolerant fuel concepts. For a high-chromium FeCrAl, similar to Kanthal APMT, most of the thermal neutron absorption in the cladding comes from ^{56}Fe (66%) and ^{53}Cr (15%) [11]. Additionally, ^{53}Cr could be isotopically de-enriched from the cladding alloy, thereby slightly reducing the reactivity penalty. Several previous modeling analyses were performed that consider changes to the fuel mass, cladding thickness, and fuel enrichment [12, 13, 14, 15].

Compared with Zircaloy, FeCrAl alloys exhibit increased hydrogen permeation because they have a body-centered cubic crystal structure [16]. Increased hydrogen permeation may lead to concern due to an increased concentration of tritium (formed during tertiary fission in the fuel) being released into the coolant. Although forming an alumina layer by preoxidizing the FeCrAl cladding may create an effective barrier to release, this layer must be formed on the cladding's interior because it could dissolve in the hydrogenated water chemistry of a boiling-water reactor [17]. Although preoxidation and liner materials may change the mechanical response of the cladding tube, they are not considered in this work.

Because many of the aforementioned challenges in material performance may be overcome, this work focuses on the utilization of FeCrAl cladding (specifically C26M) under simulated loss-of-coolant accident (LOCA) conditions using finite element modeling techniques. Specifically, this work targets the high-temperature and high-pressure conditions that a cladding tube could experience during an anticipated accident scenario to better understand the cladding failure behavior. C26M is a 12% Cr, 6% Al ferritic

alloy that is being considered as a replacement for Zircaloy cladding. C26M is a promising FeCrAl variant because it maintains desirable corrosion resistance despite its reduced chromium content. Tension tests were performed on unirradiated samples of C26M at various temperatures to determine the viscoplastic behavior of the alloy, and heated and pressurized tube rupture tests were conducted to determine the failure behavior [18]. Constitutive properties of C26M were implemented into the BISON fuel performance code along with representative conditions from the cladding rupture tests to simulate the cladding.

This analysis consisted of three separate phases: (1) the development of constitutive properties at temperatures and stresses relevant for C26M cladding burst testing, (2) a comparison of the cladding model with the simulated LOCA experiment, and (3) a scoping calculation with Zircaloy-4 to identify performance differences with C26M under these burst conditions.

2. FeCrAl (C26M) Alloy Properties

The C26M FeCrAl variant was chosen as the candidate thin-walled cladding tube to be tested at the Severe Accident Test Station (SATS) at Oak Ridge National Laboratory (ORNL). C26M is a second-generation FeCrAl alloy resulting from years of alloy development and testing in the US Department of Energy's Fuel Cycle Research and Development Advanced Fuels Campaign [19]. C26M nominally consists of Fe-12Cr-6Al-2Mo-0.2Si-0.03Y wt % and capitalizes on the high-temperature steam oxidation resistance of the alloy family while enhancing the mechanical properties over the previous generation of FeCrAl variants. To simulate the cladding tube under simulated LOCA conditions, relevant constitutive properties need to be identified and implemented into the finite element framework.

Because the C26M alloy is relatively new, mechanical testing for the alloy has been focused on properties anticipated to vary significantly from the properties of other alloy variants that have undergone more thorough experimental testing. Although a comprehensive set of material thermal and mechanical properties is not available for C26M, properties expected to dominate the alloy behavior under LOCA conditions—specifically, thermal creep and plasticity—have been investigated. The thermal and elastic properties of C26M are assumed to be very similar to the C35M variant, which has a nominal composition of Fe-13Cr-5Al-2Mo-0.2Si-0.05Y wt % [20]. Because these burst tests were not conducted on irradiated cladding tube samples, only unirradiated properties were considered in this work.

2.1. Thermal Creep

A thermal creep model for C26M was developed using previous data targeting the creep performance of the alloy [21]. Previous thermal creep models developed for other FeCrAl variants show reasonable agreement with creep data by using a fit to a power-law creep model [20]. Thus, this form, shown in Eq. (1), was used to develop a C26M-specific model. The creep strain rates from work by Joshi et al. were used to develop coefficients for this power-law creep model [22]:

$$\dot{\epsilon}_{th.} = A\sigma^n \exp\left(\frac{-Q}{RT}\right) \tag{1}$$

where A is the creep prefactor (4.0×10^{-31} s^{-1}), n is the unitless stress exponent (5.1), Q is the creep activation energy (289.0 kJ/mol), and R is the gas constant (8.314 J/[mol·K]). Figure 1 shows a comparison of the thermal creep rate of C26M and C35M with temperature, based on various applied stresses. Thermal creep for C35M is described, as specified by Terrani [23], using the same power-law form with coefficients specific to C35M. For temperatures above 600°C, coefficients from creep testing for FeCrAlloy by Saunders et al. [24] are used in the creep strain model, which extends up to 1373 K. This figure shows that, under equivalent conditions, the creep rate for C26M is expected to be much lower (by 1–2 orders of magnitude) than the creep rate for C35M.

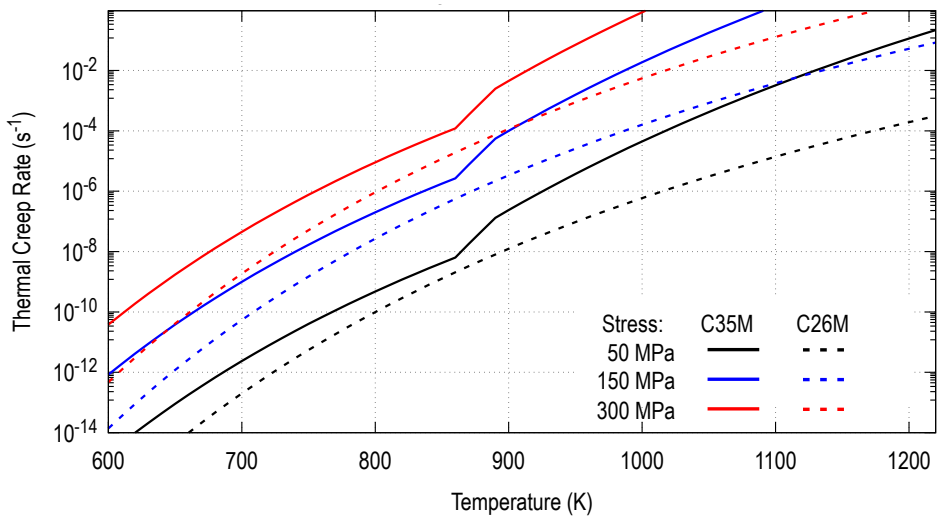

Figure 1: The C26M FeCrAl variant exhibits lower thermal creep strain rates than C35M at burst-relevant temperatures and stresses.

2.2. Plasticity

The stresses encountered during a simulated LOCA are expected to surpass the yield strength (YS) at elevated temperatures and cause significant plastic deformation. Therefore, to calculate the material deformation, a description of the plastic behavior of the alloy is necessary. Because the elastic behavior of candidate cladding FeCrAl alloys has been relatively insensitive to minor alloy composition changes, the elastic behavior variation with temperature is described using models for ORNL FeCrAl alloys [25].

Raw stress–strain curves from C26M tensile testing, as performed by Bell et al. [18], were analyzed. Tests were performed in pairs at seven different temperatures (20°C, 200°C, 400°C, 500°C, 600°C, 700°C, 800°C) at a strain rate of $10^{-3}\,\mathrm{s}^{-1}$. Figure 2 shows the raw tensile data for these tests (illustrated in black) along with a smoothing function (red in the figure) to remove the noise from the extensometer measurements. Both curves for each temperature were averaged in stress and strain space to generate a single tensile curve that reflects the engineering stress and strain of the alloy at each temperature. True stress and strain conversions were applied to the modified tensile curves, which were required for use later in the fuel performance code. Figure 3 shows the engineering stress versus strain for each temperature (solid) and the true stress versus strain (dashed line) at each temperature.

Because the elastic response of the alloy was calculated separately, only the plastic portion of the behavior was necessary (i.e., only values above the yield point of the alloy were used). To further simplify the plasticity model, failure was assumed to occur conservatively at the ultimate tensile strength (UTS) (discussed further in the next subsection), and values beyond this point were discarded. Figure 4 shows the resulting stress versus plastic strain curves. These curves allow interpolation of the alloy with increasing temperature during plastic deformation.

2.3. Failure Stress

To calculate material failure during the simulated burst tests, an explicit failure criterion must be specified. Multiple failure criteria have been established for use in high-temperature tests of cladding materials. Typically, simulated LOCA tests use a *burst* stress that is fitted to prior burst tests; this burst stress provides an accurate but shallow understanding of the underlying material failure mechanism [26]. Similar models have been developed for FeCrAl cladding variants under burst conditions [13, 7].

The focus of this work was to develop a constitutive description of C26M, which does not require prior burst testing to be evaluated. Therefore, the UTS of the alloy is proposed as a more universal failure criterion. Under the loading conditions of the simulated LOCA test, truncating the plasticity curves to the

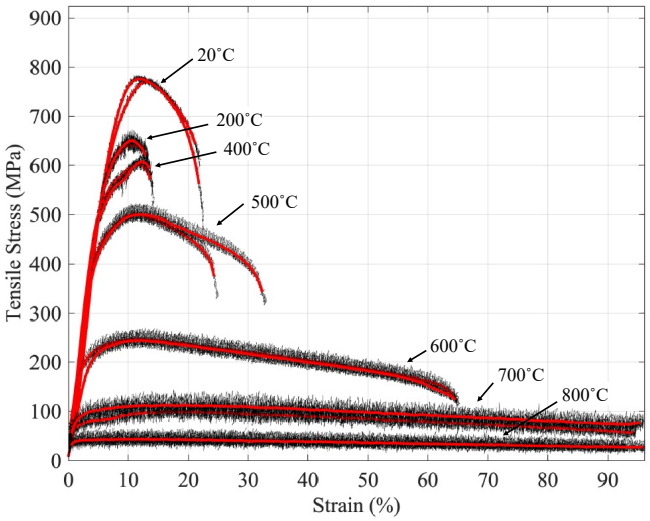

Figure 2: Raw (black) and smoothed (red) C26M tensile response at 20°C, 200°C, 400°C, 500°C, 600°C, 700°C, 800°C.

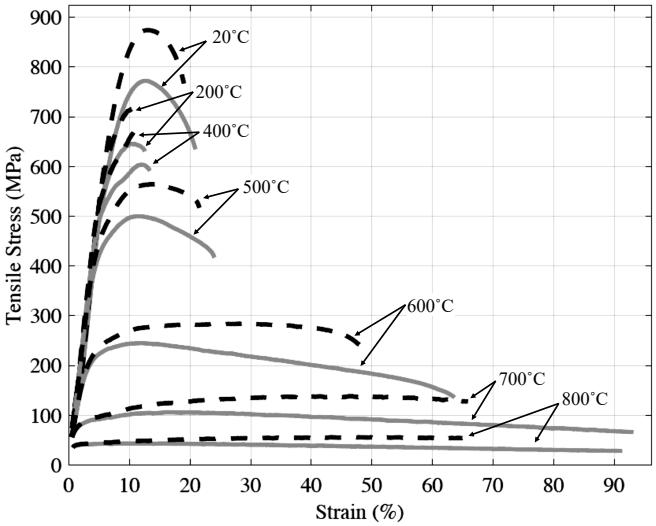

Figure 3: Engineering stress versus strain (solid) and true stress versus strain (dashed) C26M tensile curves at 20°C, 200°C, 400°C, 500°C, 600°C, 700°C, 800°C.

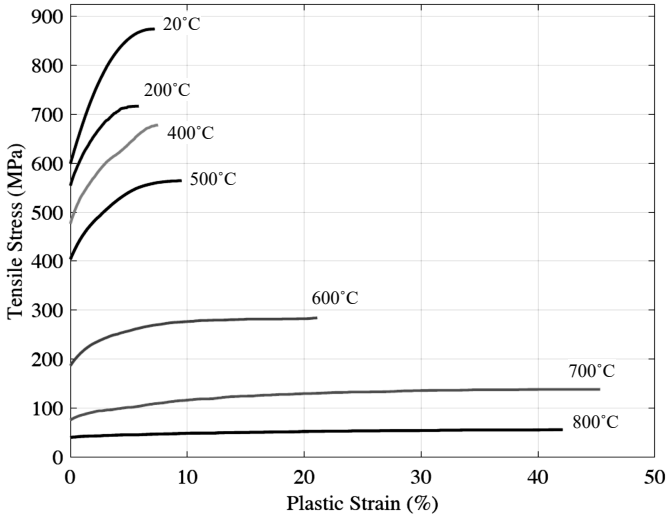

Figure 4: True stress and strain curves for the plastic deformation portions of the tensile curves (YS to UTS).

UTS is expected to be only slightly conservative because the material is expected to fail by plastic instability very soon after reaching the UTS. The true YS and UTS are shown in Figure 5. Values for these curves were generated from the tensile tests, as shown in Figure 4. An additional point was added to both the UTS and YS data as an extrapolation to the expected loss of strength at the high temperatures at which the alloy approaches its melting point. Specifically, both the UTS and YS are assumed to reach zero at 1500 K. In the absence of data at higher temperatures, this point was expected to provide a more conservative estimate than the alloy melting temperature, 1773 K for APMT (a similar FeCrAl alloy).

Although the irradiation hardening behavior of FeCrAl alloys (due to α' precipitation of chromium) is established [27], these effects were not considered in this model because the simulated LOCA test and the tensile specimen were both unirradiated.

3. Modeling Approach

A finite element fuel performance code was used to simulate the cladding tube behavior under simulated LOCA conditions in the SATS at ORNL. For these simulations, C26M material properties, cladding tube geometry, and testing conditions were implemented into the BISON code. The BISON code, in conjunction with this modeling approach, has previously been used to analyze burst tests of multiple cladding types, including coated and uncoated Zircaloy cladding [28] and oxide dispersion-strengthened FeCrAl [29].

3.1. The Severe Accident Test Station

Data generated from experiments performed in the SATS at ORNL were used to model the cladding conditions during the transient scenario [30]. During these experiments, a pressurized cladding tube specimen was heated inside a quartz tube using four infrared heating elements until the cladding ruptured. These cladding tube samples were nearly 12 in. long and had an alumina rod (8 mm outer diameter) that spanned from the fittings on either end through the center of the tube. The cladding tubes used were 380 μm thick with an inner diameter of 9.52 mm. Details on the specific setup for the SATS LOCA furnace are available elsewhere [31, 18].

In these tests, a pressure transducer was used to measure the pressure of the argon gas (in situ), which was set and sealed before heating. This measurement was performed using an external gas system that included a gas tank, a pressure regulator, a shutoff valve, and the pressure transducer. The gas system was connected to the cladding tube by a Swagelok fitting. The cladding was instrumented with four thermocouples: three distributed along its rear axial length and one placed at the midplane of the front of the tube (rotated 180°

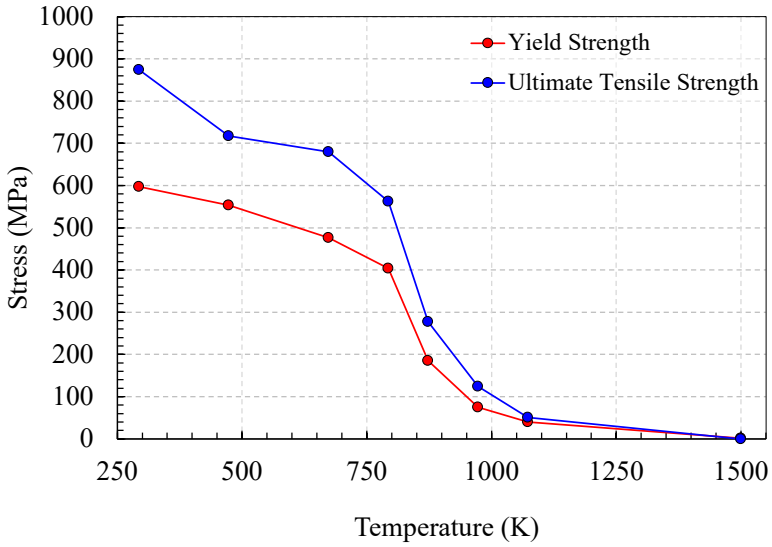

Figure 5: True YS and UTS used to define the limits of the plastic behavior and failure of the C26M alloy.

azimuthally from the first three thermocouples). The cladding tubes were heated to a temperature of 573 K (300°C) and held at that temperature for approximately 5 min. The cladding tubes were then ramped at approximately 5°C/s, as determined by a control thermocouple. In this case, the thermocouple at the midplane of the rear of the tube was used.

As the argon gas expands during the heating phase, the cladding tube will eventually balloon and burst. The exact time of cladding burst was determined using the data from the pressure transducer, which recorded a rapid depressurization upon burst. For these experiments, flowing steam heated to 673 K (400°C) was injected into the chamber to more realistically simulate the environment present during a LOCA. The cladding was then heated to approximately 1473 K (1200°C) and held at that temperature for 5 min. Finally, the furnace was deactivated, and the cladding was allowed to cool naturally until the cladding control thermocouple reached 873 K (600°C), at which point the flowing steam was shut off and the tube was quenched in distilled water at room temperature. The thermocouples arrayed along the rear of the cladding tube were placed in the central 4 in. (approximately 10.2 cm) of the tube length. For all of the experimental tests considered in this work, the middle thermocouple was approximately 6 in. (approximately 15.2 cm) from the bottom of the cladding tube, and the top and bottom were 2 in. (approximately 5.1 cm) above and below, respectively. Figure 6 illustrates the thermocouple locations and the most commonly observed burst location. Burst was most commonly observed on the rear of the tube between the central and bottom thermocouple locations. This observation is important because the cladding is expected to experience the greatest deformation in the hottest region. The only variation between the tests discussed here was the difference in initial internal pressures.

Data acquired over time from a typical burst test are shown in Figure 7. The left-hand axis of Figure 7 shows the temperatures recorded by the four thermocouples over the first 700 s of the burst test. This specific test was performed for a C26M cladding tube with an initial pressure of 900 psi (approximately 6.2 MPa). The right-hand axis shows the data recorded by the pressure transducer over the same period of time. The pressure initially increased with the gas temperature as the cladding was heated to the first holding stage. This pressure increase did not necessarily correspond directly to the cladding temperatures because additional gas volume in the gas system was present outside the cladding tube sample. After the holding period, the cladding temperature was ramped to simulate the LOCA transient. Rupture occurred at approximately 560 s for this sample, as indicated by the rapid decrease in pressure and the corresponding large change in cladding temperatures. This temperature shift was driven by the release of gas from

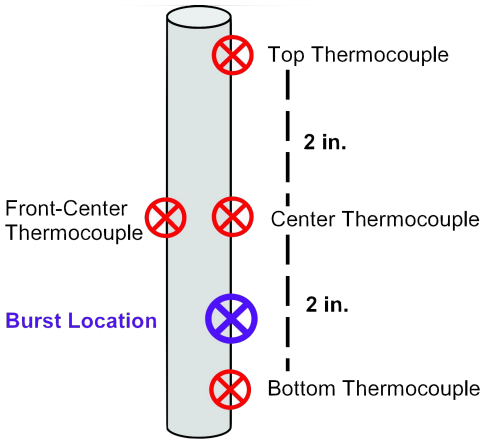

Figure 6: Schematic showing thermocouple placement and the most common burst location on the center 4 in. (approximately 10.2 cm) section of the 12 in. (approximately 30.5 cm) cladding tube specimen used in the SATS (as reproduced from [28]).

portions of the gas system that were outside the furnace (and were therefore cooler than the cladding). This work focused only on the bursting behavior of the cladding tube, so the subsequent heating phase, high-temperature phase, cooling phase, and quench phase were omitted from the simulation conditions.

Tube initial pressures for this test series were varied from 200 to 1200 psi (1 to 8.3 MPa). All tests were performed using the same geometry and setup described above.

3.2. The BISON Fuel Performance Code

BISON is a finite element analysis tool for nuclear fuels, which is built on the Multiphysics Object Oriented Simulation Environment (MOOSE) framework [32]. MOOSE employs a Jacobian-free Newton–Krylov method to solve systems of coupled nonlinear partial differential equations [33]. The modularity and expandability of the MOOSE framework allows BISON to incorporate a host of material property models and behavioral models for integral fuel performance modeling. The model developed for this work leveraged existing capabilities and included material-specific constitutive properties, cladding tube geometry, and experimental operating conditions discussed above [34].

Specifically, previously developed constitutive properties for the alumina rod were used for these simulations. The material properties described in the previous section were used for the FeCrAl cladding. Purely elastic and thermal properties (thermal conductivity, specific heat capacity, and thermal expansion) were used to model the alumina rod [35]. The rod was assumed to have no direct mechanical effects on the cladding tube, but it may serve as a heat sink during the heating phase, thereby affecting the temperature of the tube. Therefore, heat transfer between the alumina rod and the tube across the gap region, and heat conduction within the rod and tube, were all modeled. Model predictions were compared directly with the cladding engineering stress (calculated using the internal pressure) and the cladding temperatures because the in situ true values were not available. Capabilities are being developed to measure the in situ true strain spatially across the tube during the experiment using digital image correlation and additional enhanced instrumentation [36, 37]. Follow-on modeling work may incorporate data from experiments conducted using these capabilities to allow for a more direct comparison between the observed behaviors and simulation predictions.

Simulations were conducted using 180° cladding tubes in 3D. Zero-displacement boundary conditions were applied to the axial faces of the sectioned tube and to the bottom of the tube to prevent rigid body motion. Cladding oxidation was not modeled because it was expected to remain at a negligible thickness (<1.3 μm) at the burst temperatures and times considered in these tests [38]. The half-rod symmetry used in these simulations reduced computational expenses while fully incorporating the azimuthal and axial temperature variations observed in the tests. The cladding end tubes were assumed to be sealed to simplify the

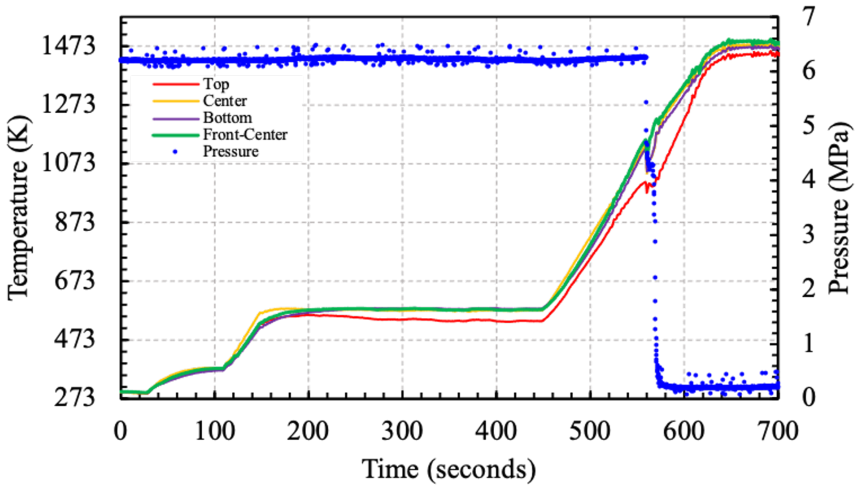

Figure 7: Cladding tube burst is identified in typical SATS burst tests by a rapid drop in pressure (right axis) inside the tube (blue) and a slight depression in temperature (left axis) at the four thermocouple locations along the cladding tube: rear-top (red), rear-center (yellow), rear-bottom (purple), and front-center (green).

calculation of the gas volume inside the tube. The gas volume was taken to be the sum of two contributions: (1) the volume inside the tube itself, which increases the internal pressure as it heats and expands, and (2) the volume of the remainder of the gas system—including lines, fittings, valves, and the pressure transducer—which was held at room temperature. The miscellaneous volume was independently calibrated for each series of tests based on the measured increase in pressure during the temperature ramp. This calibration accounted for variations in gas system volume between tests. This model effectively serves as a gas reservoir that dampens pressure changes within the cladding tube because the volume and temperature of the reservoir do not change, but the pressure remains in equilibrium with that of the cladding tube. The only external conditions applied to this model were the temperature obtained from the thermocouples and the initial pressure of the gas system. Section 3.3 describes the procedure by which the cladding surface temperatures were generated from the thermocouple data for each test. These temperatures were applied to the cladding surface using time-varying Dirichlet boundary conditions. Because the simulations assessed the volume, temperature, and pressure of the internal gas together from room temperature, the internal pressure was set to closely match the pressure of the burst experiments during the first holding period after the pressure regulator was set, the gas valves were closed, and the tube was sealed. These simulations operated through the first holding period until the heating phase and were terminated when the cladding failure threshold was reached.

3.3. Cladding Surface Temperature Development

With the material-specific constitutive properties implemented into BISON, boundary conditions based on the experiments were derived and implemented. The intention was to validate BISON predictions obtained using the material-specific properties against experimental measurements to ultimately elucidate the mechanisms and properties responsible for the observed failure behaviors.

The conditions available from the experiment included time-resolved thermocouple temperatures, time-resolved internal pressure readings, and post-test cladding strain profiles. The 3D cladding surface temperatures were developed from the thermocouple measurements and were applied directly to the cladding surface to enable direct comparisons between simulated and observed behaviors. The initial pressures from each burst test were used to define the initial pressure conditions for the simulations.

The thermocouple data from the SATS experiments were used to derive continuous axial and azimuthal surface temperatures for application to the full 3D cladding model, thereby increasing its spatial fidelity. In the past, the temperatures between thermocouple locations were simply interpolated linearly. However,

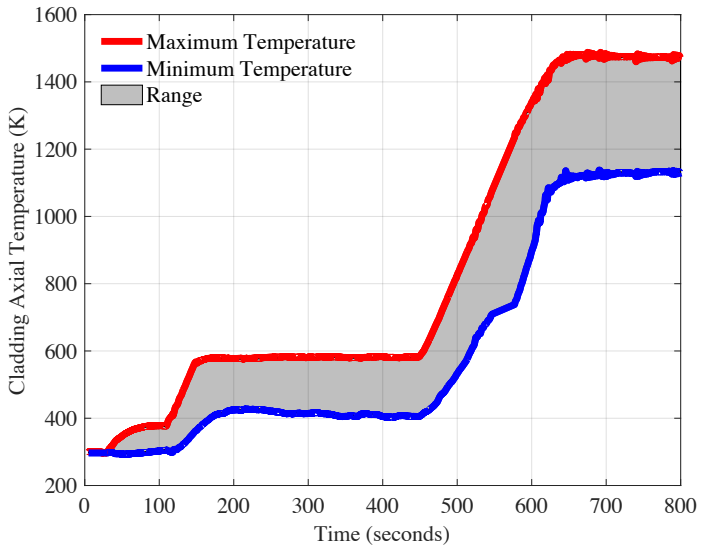

Figure 8: Example of maximum and minimum cladding tube temperatures and the range of axial temperatures generated by fitting a fourth-order polynomial to the experimental thermocouple data.

because cladding burst does not necessarily occur at the thermocouple locations, this approach may overlook the actual peak temperature of the cladding and therefore interpret the burst temperature incorrectly. The burst locations observed in these tests exhibited a degree of reproducibility, suggesting that the observed failure behaviors are not dominated by the presence of preexisting flaws or sample preparation. Failure can therefore be attributed to the thermal and stress conditions to which the samples were exposed. Furthermore, because the complete surface temperature is needed to accurately calculate cladding pressure evolution owing to gas expansion, this refined method serves to improve the pressure calculation.

To account for axial temperature variation, a fourth-order polynomial was fit using the thermocouple temperatures as constraints. This polynomial was also fit to the cladding temperatures at the ends of the tube. These temperatures have been determined to fall within 60%–80% of the nearest thermocouple temperature. This estimate is based on previous tests in the SATS, which used a fiber-optic temperature sensor. Although this may be a significant approximation, the ends of the cladding tube are known with certainty to be much cooler than the middle section because of the tube placement within the furnace. Therefore, the ends of the cladding tube do not experience significant deformation owing to thermal creep.

Figure 8 shows the range of temperatures generated from these continuous functions. The fourth-order fitting method was applied at each time point in the experimental data series (in intervals of 0.1 s). Figure 8 shows the full range of the maximum and minimum temperatures encountered during the experiment. For each of these tests, the jump in the burst temperatures due to release of the stored gas at the time of burst was cut out. The thermocouple temperature increase over time is linearly interpolated over these times. This is to ensure that the future prediction was not influenced by the temperature change from the sudden release of gas through the opening of the rupture.

Finally, the azimuthal thermocouple data were compared with the corresponding middle thermocouple data to calculate a relative azimuthal thermocouple factor, which indicates the relative temperature difference between the front and back of the cladding tube. Figure 9 shows an example of the azimuthal thermocouple factor. Therein, the rear of the cladding was consistently hotter than the front side (as indicated by a value lower than one). The azimuthal temperature difference was incorporated into the combined cladding surface temperature function (axial and azimuthal) using a cosine function that varied along the outer circumference of the tube. This assumption produced a uniform azimuthal variation that may not have been entirely accurate for these experiments but was expected to be reasonable in the absence of more

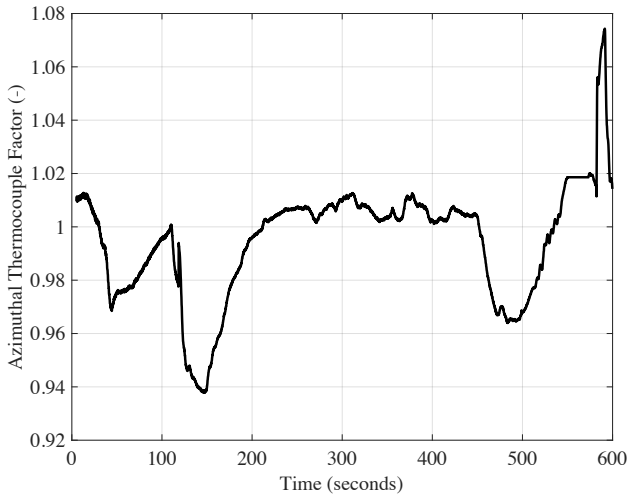

Figure 9: The azimuthal thermocouple factor, which indicates the relative temperature variation between the front and back thermocouples at the axial midplane of the tubes. This was used to define the temperature variation around the cladding circumference, and values greater than one indicate that the front thermocouple reading was greater than that of the rear thermocouple.

thorough characterization of tube surface temperatures.

Finally, the axial temperature profile and the azimuthal variation were combined to generate a full 3D temperature surface for the cladding. This surface served as an input in transient simulations. Boundary conditions for the 3D cladding model were generated from each cladding burst test for use in BISON. Figure 10 shows an example that illustrates the surface temperature derived for a typical cladding tube. This example shows the surface temperature at the burst temperature for a C26M burst test with an initial pressure of 400 psi. A hot spot in the cladding formed along the front, near the lower span of the cladding tube. This local increase in temperature led to a localized increase in the creep strain rate and subsequent cladding failure in that location.

Finally, the tube internal volume used in the simulations was calibrated to match the pressure evolution observed during the experiment. This calibration helped to account for the large amount of gas that was held in the fixtures that hold the cladding tube and the gas lines that run to the pressure regulator and shutoff valve. Figure 11 shows examples of the pressure histories from a simulation and the corresponding experiment. In this particular case, the cladding tube test had an initial pressure of 7.4 MPa. During the holding and heating phases, the pressure increased as the temperature increased. Calibrating the internal volume allowed the stress state of the cladding tube to be matched with the temperatures from the experiment to provide a more accurate calculation of the conditions present at the point of cladding failure. The simulated temperature and pressure at burst were compared with the experiment measurement. In six total comparisons, initial pressures ranged from 1 MPa to 8 MPa.

Figure 11 shows the pressure evolution associated with the cladding tube during this same simulation. The initial pressure was 7.4 MPa (shown in blue), but the data began at nearly 7.4 MPa (shown in red). The pressures through the holding phase were slightly different because of the different starting pressures, but the pressure in the experiment slowly increased to reach a similar value before the heating phase. This was assumed to have occurred because of the heating of the connected equipment, which may have in turn heated the gas in portions of the gas system volume outside the cladding tube. The pressure in both the simulation and the experiment increased similarly as the heat up phase began. The simulation was terminated prior to the point at which extensive deformation would occur, so the pressure data do not show the same shoulder observed in the experiment before the cladding ruptures. This is due to both the high-temperature cladding creep model and the failure criteria. Although the evolution of the cladding deformation was expected to be somewhat different, the calculated and measured times to failure and the temperatures were quite similar,

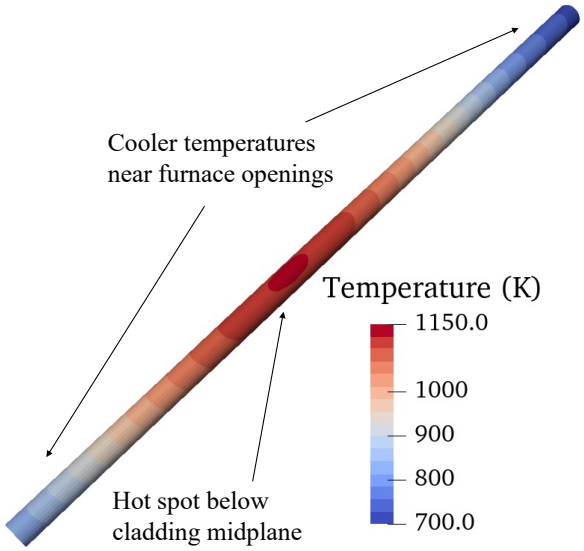

Figure 10: Re-creation of the cladding surface temperature in 3D using the axial and azimuthal temperature functions. In this case, a hot spot formed on the front of the cladding below the midplane just before burst was calculated. Cooler temperatures near ends of the cladding tube were due to the vicinity of the furnace openings.

indicating satisfactory boundary conditions supplied to the model and good general performance.

4. Initial Analysis

The previously mentioned process was used to develop full 3D cladding surface temperatures at each data measurement point for each of the six cladding burst tests, along with calculated external volumes, which represent the fill gas not contained in the cladding tube. Figure 12 shows the resulting stresses and temperatures at burst for the cladding burst tests and simulations. The BISON simulations consistently underpredicted the burst temperature by up to approximately 110 K, or approximately 20 s at the targeted 5°C/s heating rate. On average, these calculations are approximately 76 K below the measurements. The peak reported creep strain for these simulations remains below 0.03%, and plasticity dominates the deformation of the cladding.

Notably, to remain consistent with the experimental measurement, the temperatures reported using BISON reflect the peak thermocouple temperatures rather than the actual peak temperature. As a side note, the predicted peak temperatures range from 5 to 15 K greater than the highest thermocouple temperatures at burst. Although this difference will not immediately affect this comparison, it is an important consideration for the data and models generated using burst tests with this instrumentation setup.

Because these temperatures lie in or near the region of the tensile data which is interpolated from the last tensile curve to melting, the tensile properties rely on both the last data point and the assumption that the material strength decreases linearly to a temperature of 1500 K (as shown in Figure 5). This result is due to the cladding plasticity model as the material approaches high temperatures. In this case, the strength of the cladding at high temperature drops significantly when above approximately 1000 K. Although these data were derived from tensile tests, the tensile strength was investigated again at the highest data points to confirm this observation.

5. Improved High-Temperature Plasticity

New tensile tests were performed to test the behavior at the peak temperature possible in the high-temperature extensometer. Specifically, new tests were performed at 700°C and 800°C. In this case, alloy

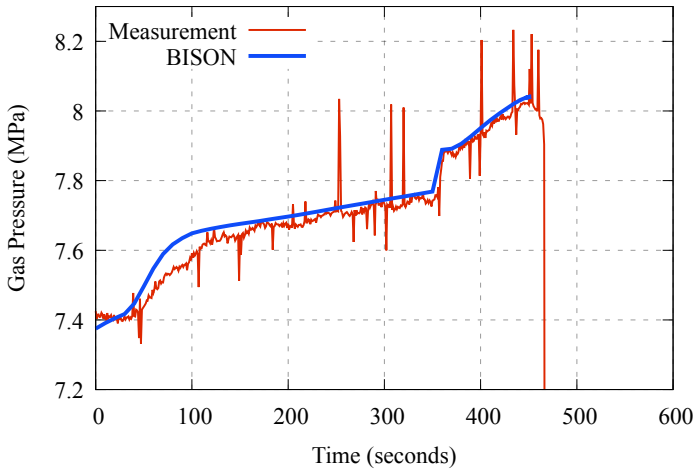

Figure 11: The pressure calculated by BISON (blue) agrees well with the measured pressure (red) and uses a calibrated initial internal volume along with the tube internal volume to determine the amount of gas to model the pressure evolution under the prescribed temperature conditions.

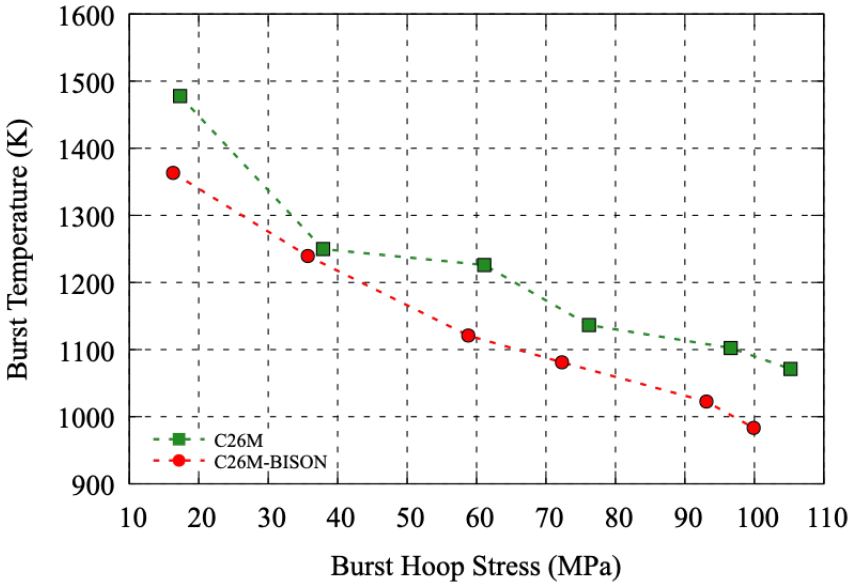

Figure 12: BISON calculates cladding failure (shown in red) at burst temperatures nearly 100 K lower than experimentally measured burst temperatures (green).

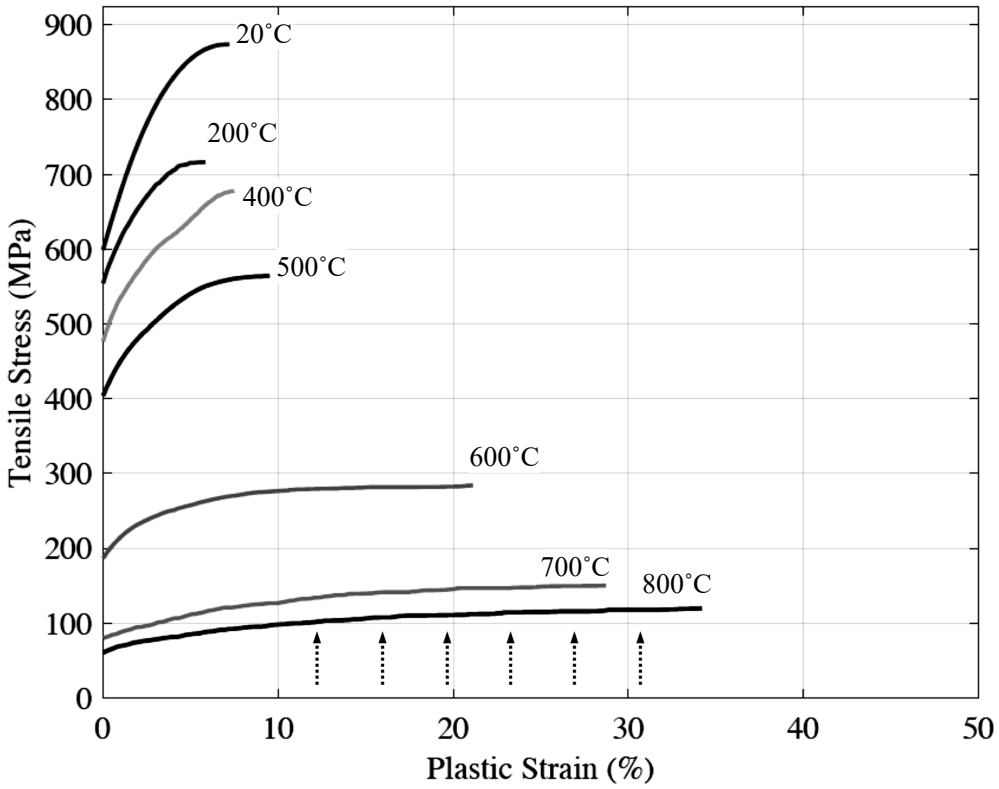

Figure 13: New plastic deformation curves, obtained at 700°C and 800°C, were implemented to demonstrate the effect of the high-temperature holding time and show increased strength and reduced elongation over the previous iteration.

recrystallization or thermal softening was hypothesized to have occurred during the high-temperature hold before the test started which possibly generated tensile strengths below those encountered in the simulated LOCA test. This finding was confirmed by two additional tensile tests that used much shorter hold times at the test temperature. The same process used to generate the original C26M plasticity model, discussed in Section 2.3, was used to implement the new data for the 700°C and 800°C tests. Figure 13 shows the resulting model. Notably, the new plastic tensile curve for the 700°C test showed only slightly increased UTS (approximately 20 MPa) compared with the original model (Figure 4), and elongation decreased by nearly 17%. The new 800°C tensile test showed a more substantial increase in UTS (approximately 60 MPa), and elongation decreased by only 7%.

Figure 14 shows a comparison of the YS and UTS for the different tensile test iterations with temperature. Although the difference in YS for the new model is modest, the UTS shows a substantial increase. Because this plasticity model is interpolated to 1500 K, just like the previous iteration, this will fundamentally increase the burst temperature calculation in the interpolation region (1073–1500 K).

The new plasticity model was implemented into BISON, and each burst test was simulated. The results of these simulations using the updated plasticity model are shown in Figure 15. Compared with previous simulations, the hoop stresses calculated using the updated model were slightly increased—shown in Figure 15 as a shift to the right for nearly all points. Nearly all simulations showed improved agreement with the simulated LOCA measurements. The only exception was the test with the lowest initial fill pressure; this test reached the highest burst temperature. Compared with the previous iteration of simulations, this test actually showed a slightly higher burst stress but a lower temperature. By using the improved model, these simulations on average showed an improvement of approximately 26 K.

Given the favorable comparison of the simulations and experiment, a short parametric evaluation was

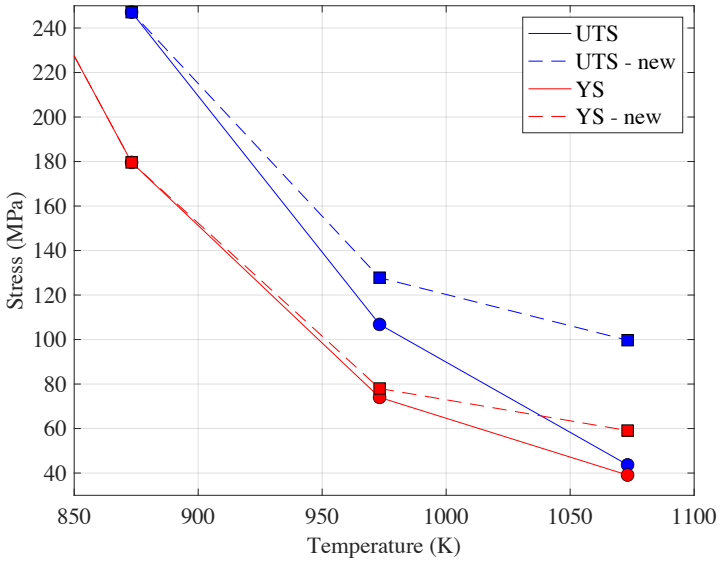

Figure 14: New tensile tests with shorter high-temperature hold times (dashed lines) show increased YS (red) and UTS (blue) over the original values (denoted by solid lines).

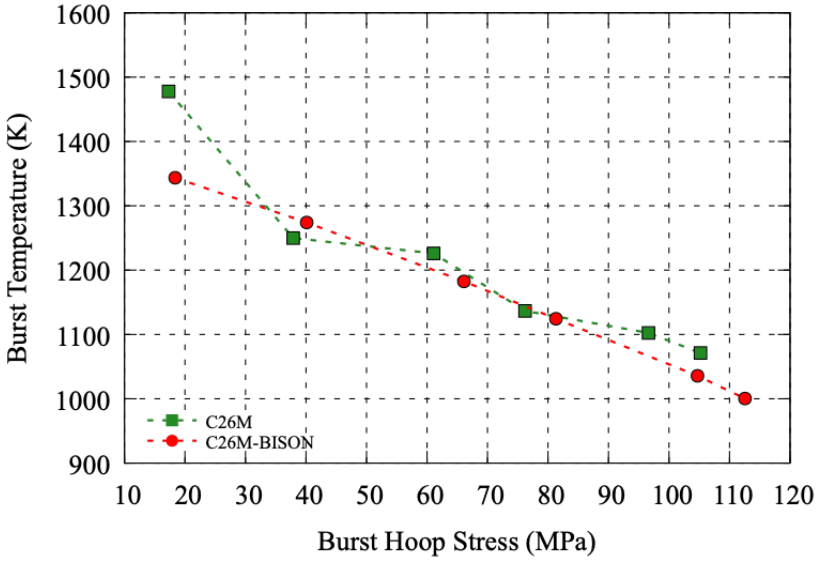

Figure 15: Using the updated plasticity model, burst temperatures calculated using BISON (shown in red) showed an improvement over the previous iteration and agreed more closely to the experimentally measured temperatures (green).

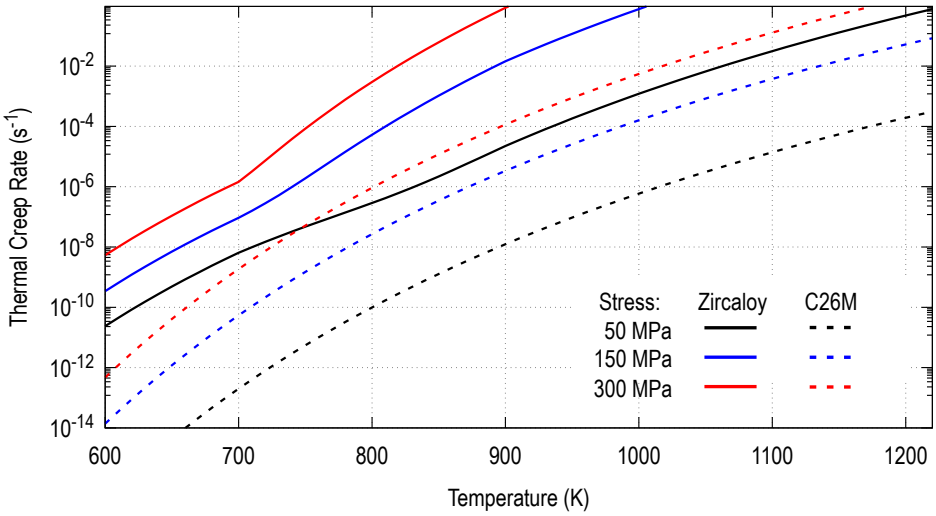

Figure 16: Zircaloy (solid) thermal creep strains remained orders of magnitude larger than those associated with C26M (dashed) for all stresses and temperatures considered here.

performed to identify the impact of the C26M cladding over traditional Zircaloy-4 using various initial pressures to develop burst temperature versus strain curves.

6. Burst Comparison with Zircaloy Cladding

Driven by the significant interest in using FeCrAl cladding as a replacement for Zircaloy, these simulations were extended to make a direct comparison between the two cladding types under high-temperature conditions. The Zircaloy tubes used in this analysis were 570 µm thick and 12 in. long; these tubes used the same outer diameter as the previous analysis (10.24 mm). To perform this analysis, Zircaloy and C26M cladding tubes were each simulated using the same temperature boundary conditions; however, the initial internal pressures were varied in 1 MPa increments. Each cladding tube was simulated until failure, and the burst temperature margins were compared.

6.1. Zircaloy-4 Properties

For the Zircaloy cladding, elastic, thermal, creep, and plasticity properties already distributed with the BISON code were used. The elastic modulus, Poisson's ratio, thermal expansion strain, thermal conductivity, and specific heat were all calculated for the zirconium-based alloys using correlations from MATPRO [39]. The plasticity model implemented was described by Geelhood et al. [40]. The thermal creep model was divided into a composition-specific, low-temperature correlation [41, 42] and a high-temperature, phase-dependent creep model [43]. The high-temperature thermal creep model for Zircaloy uses the same model form as the C26M, as shown in Eq. (1) with parameters that vary based on the calculated phase composition. The parameters and the phase model were determined from a previous work on the behavior of cladding during high-temperature transients [44] and described by Massih et al. [45, 46, 47]. The aforementioned models for the zirconium-based cladding materials are distributed with the BISON code by default.

Figure 16 shows a comparison of the Zircaloy creep model versus the C26M alloy. This illustration shows the nearly 2–4 orders of magnitude greater creep strain rates expected for Zircaloy compared with C26M under equivalent conditions.

In this analysis, the Zircaloy cladding failure used two separate criteria [48]: a cladding overstress criterion and a creep strain rate limit criterion. The cladding overstress criterion was used when the cladding reached a hoop stress limit, which is a function of the cladding phase and the oxygen content [43, 49]. The creep strain rate limit criterion was used when the creep rate reached $\tilde{2}.78\%/\mathrm{s}$; this rate is based on previous work

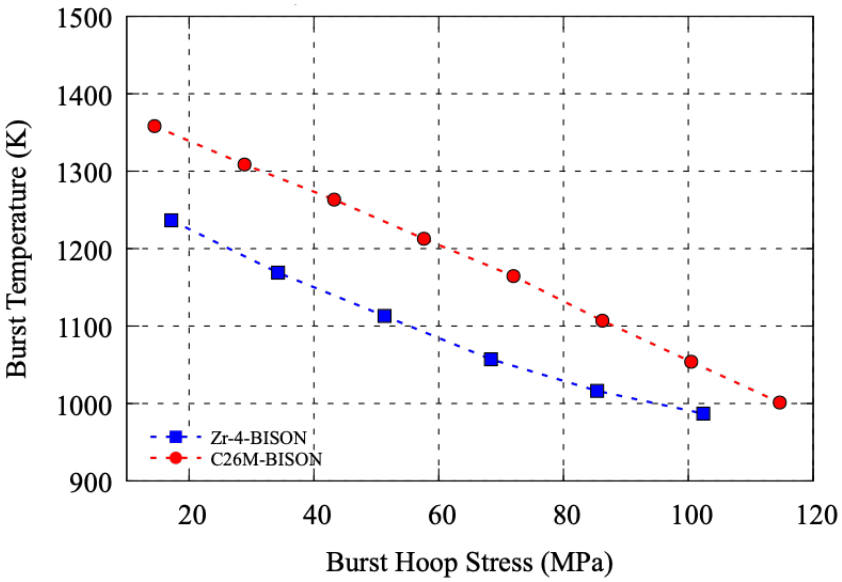

Figure 17: Compared with the corresponding Zircaloy cladding tube, C26M exhibits a nearly 100 K burst temperature increase.

that modeled plastic instability in fuel performance codes [50]. At this point, the cladding is assumed to undergo plastic instability and begins to rapidly deform to failure.

6.2. Burst Temperature Comparison

Simulations were performed using an initial pressure of 1 MPa, which was then increased in 1 MPa increments. The burst temperatures and cladding stresses from this sensitivity analysis are shown in Figure 17. This comparison shows that, although the FeCrAl cladding was substantially thinner than the Zircaloy (190 µm), the burst temperatures remained nearly 100 K higher throughout much of the range considered here.

Although these tests demonstrated superior performance of the alloy under controlled conditions, when used in light-water reactor applications, the greater creep resistance of the alloy is expected to affect the steady-state behavior of the alloy. The FeCrAl-clad fuel pellets are expected to exhibit increased fission gas release as a consequence of higher temperatures from slower gap closure. Increasing the initial pressure for the FeCrAl may lead to similar burst times to Zircaloy under LOCA conditions.

7. Summary and Conclusions

In order to better understand the plastic behavior and failure of C26M under simulated LOCA conditions, cladding burst experiments were performed in the SATS facility at ORNL. These experiments were simulated using the BISON fuel performance code. This modeling effort utilized constitutive properties for the C26M alloy based on previous testing of similar FeCrAl alloys, as well as new plasticity, creep, and failure models generated using experimental data. The models were then implemented into the BISON fuel performance code to simulate the LOCA tests. Thermocouple readings from the tests were used to develop 3D cladding surface boundary conditions using composite axial and azimuthal profiles.

Results from these six simulated LOCA tests exhibited consistent underprediction of burst temperatures compared with the temperatures measured during the tests. This discrepancy was driven by the differences in the material properties and the failure stress assumed in the model; these parameters were subsequently reinvestigated. Analysis of the tensile property acquisition indicated that the cladding tubes did not experience the same high-temperature hold as the tensile specimens. This extended hold was used to ensure an equilibrium temperature was reached in the samples during the tensile tests. Therefore, new tensile

tests were performed at the highest temperatures using a temperature ramp similar to the simulated LOCA experiments and a decreased holding time. The resulting tensile curves showed a substantial increase in the UTS of the C26M alloy (nearly 80%). This increase indicates a microstructural change in the C26M cladding, that occurred during the 10 min hold at 700°C and 800°C.

Incorporating the updated tensile curves into the simulations significantly improved the agreement between the simulated and observed burst temperatures and stresses. This study was then extended to assess the burst temperature difference between standard Zircaloy-4 and C26M cladding under equivalent conditions by varying the cladding initial pressure. In this study, C26M showed an increase in burst temperature of nearly 70–130 K over Zircaloy.

These modeling predictions can be further improved by collecting high-temperature tensile data for C26M beyond the temperature ranges used in this work. Specifically, acquiring tensile properties at temperatures above 800°C would help improve simulation accuracy. Additionally, because the strain rate of the tensile test is different than that of the simulated burst test, further investigation is recommended to ensure that no significant strain-rate effects are included in the data used to generate the plasticity model.

Acknowledgments

Funding was provided by the US Department of Energy Advanced Fuels Campaign. This research made use of the resources of the High Performance Computing Center at Idaho National Laboratory, which is supported by the Office of Nuclear Energy of the US Department of Energy and the Nuclear Science User Facilities under Contract No. DE-AC07-05ID14517.

References

[1] J. Carmack, F. Goldner, S. M. Bragg-Sitton, L. L. Snead, Overview of the US DOE accident tolerant fuel development program, Tech. rep., Idaho National Lab.(INL), Idaho Falls, ID (United States) (2013).

[2] S. J. Zinkle, K. A. Terrani, J. C. Gehin, L. J. Ott, L. L. Snead, Accident tolerant fuels for LWRs: A perspective, Journal of Nuclear Materials 448 (1-3) (2014) 374–379.

[3] K. A. Terrani, S. J. Zinkle, L. L. Snead, Advanced oxidation-resistant iron-based alloys for LWR fuel cladding, Journal of Nuclear Materials 448 (1-3) (2014) 420–435.

[4] L. J. Ott, K. R. Robb, D. Wang, Preliminary assessment of accident-tolerant fuels on LWR performance during normal operation and under DB and BDB accident conditions, Journal of Nuclear Materials 448 (1-3) (2014) 520–533.

[5] K. R. Robb, Analysis of the FeCrAl accident tolerant fuel concept benefits during BWR station blackout accidents, Tech. rep., Oak Ridge National Lab.(ORNL), Oak Ridge, TN (United States) (2015).

[6] A. Strasser, J. Santucci, K. Lindquist, W. Yario, G. Stern, L. Goldstein, L. Joseph, Evaluation of stainless steel cladding for use in current design LWRs. Final report, Tech. rep., Stoller (SM) Corp., New York (USA) (1982).

[7] R. T. Sweet, G. Pastore, B. Wirth, Analysis of FeCrAl cladding performance under loss-of-coolant accident conditions, Nuclear Engineering and Design 414 (2023) 112556.

[8] N. M. George, K. Terrani, J. Powers, A. Worrall, I. Maldonado, Neutronic analysis of candidate accident-tolerant cladding concepts in pressurized water reactors, Annals of Nuclear Energy 75 (2015) 703–712.

[9] S. M. Bragg-Sitton, M. Todosow, R. Montgomery, C. R. Stanek, R. Montgomery, W. J. Carmack, Metrics for the technical performance evaluation of light water reactor accident-tolerant fuel, Nuclear Technology 195 (2) (2016) 111–123.

[10] C. A. Gayheart, NL-22-0288, Vogtle Electric Generating Plant, Units 1 and 2 Supplement to License Amendment Request and Exemptions to Allow Use of Lead Test Assemblies for Accident-Tolerant Fuel, Tech. Rep. ML23125A269, Southern Nuclear Operating Company (2023).

[11] I. Younker, M. Fratoni, Neutronic evaluation of coating and cladding materials for accident tolerant fuels, Progress in Nuclear Energy 88 (2016) 10–18.

[12] R. T. Sweet, N. George, G. Maldonado, K. Terrani, B. Wirth, Fuel performance simulation of iron-chrome-aluminum (FeCrAl) cladding during steady-state LWR operation, Nuclear Engineering and Design 328 (2018) 10–26.

[13] K. A. Gamble, T. Barani, D. Pizzocri, J. D. Hales, K. A. Terrani, G. Pastore, An investigation of FeCrAl cladding behavior under normal operating and loss of coolant conditions, Journal of nuclear materials 491 (2017) 55–66.

[14] R. T. Sweet, C. P. Massey, S. B. Bell, K. A. Kane, Wrought FeCrAl Alloy (C26M) Cladding Behavior During Burst Experiments and Performance Under LOCA Conditions, TopFuel 2022 Light Water Reactor Fuel Performance Conference (2022) 248–250.

[15] P. Aragón, F. Feria, L. E. Herranz, Modelling FeCrAl cladding thermo-mechanical performance. Part II: Comparative analysis with Zircaloy under LOCA conditions, Progress in Nuclear Energy 163 (2023) 104838.

[16] X. Hu, K. A. Terrani, B. D. Wirth, L. L. Snead, Hydrogen permeation in FeCrAl alloys for LWR cladding application, Journal of Nuclear Materials 461 (2015) 282–291.

[17] R. B. Rebak, Versatile oxide films protect FeCrAl alloys under normal operation and accident conditions in light water power reactors, Jom 70 (2) (2018) 176–185.
[18] S. B. Bell, K. A. Kane, C. P. Massey, L. Baldesberger, D. Lutz, B. Pint, Strength and rupture geometry of un-irradiated C26M FeCrAl under LOCA burst testing conditions, Journal of Nuclear Materials 557 (2021) 153242.
[19] Y. Yamamoto, B. A. Pint, K. A. Terrani, K. G. Field, Y. Yang, L. L. Snead, Development and property evaluation of nuclear grade wrought FeCrAl fuel cladding for light water reactors, Journal of Nuclear Materials 467 (10 2015). doi:10.1016/j.jnucmat.2015.10.019.
[20] K. G. Field, M. A. Snead, Y. Yamamoto, K. A. Terrani, Handbook on the Material Properties of FeCrAl Alloys for Nuclear Power Production Applications (FY18 Version: Revision 1), Tech. rep., Oak Ridge National Lab.(ORNL), Oak Ridge, TN (United States) (2018).
[21] P. Joshi, B. Kombaiah, M. N. Cinbiz, K. Murty, Characterization of stress-rupture behavior of nuclear-grade C26M2 FeCrAl alloy for accident-tolerant fuel cladding via burst testing, Materials Science and Engineering: A 791 (2020) 139753.
[22] J. Weertman, Theory of steady-state creep based on dislocation climb, Journal of Applied Physics 26 (10) (1955) 1213–1217.
[23] K. A. Terrani, T. M. Karlsen, Y. Yamamoto, Input correlations for irradiation creep of FeCrAl and SiC based on in-pile Halden test results, Oak Ridge National Laboratory (ORNL), Oak Ridge, TN (United States) (2016).
[24] S. Saunders, H. Evans, M. Li, D. Gohil, S. Osgerby, Oxidation growth stresses in an alumina-forming ferritic steel measured by creep deflection, Oxidation of metals 48 (1997) 189–200.
[25] Z. T. Thompson, K. A. Terrani, Y. Yamamoto, Elastic Modulus Measurement of ORNL ATF FeCrAl Alloys, Tech. rep., Oak Ridge National Laboratory (10 2015). doi:10.2172/1225433.
[26] F. Erbacher, S. Leistikow, Zircaloy fuel cladding behavior in a loss-of-coolant accident: a review, Zirconium in the Nuclear Industry (1987).
[27] K. G. Field, S. A. Briggs, K. Sridharan, R. H. Howard, Y. Yamamoto, Mechanical properties of neutron-irradiated model and commercial FeCrAl alloys, Journal of Nuclear Materials 489 (2017) 118–128. doi:https://doi.org/10.1016/j.jnucmat.2017.03.038.
[28] R. T. Sweet, P. Mouche, S. Bell, K. Kane, N. Capps, Chromium-coated cladding analysis under simulated LOCA burst conditions, Annals of Nuclear Energy 176 (2022) 109275.
[29] C. P. Massey, K. A. Kane, R. T. Sweet, S. B. Bell, S. N. Dryepondt, J. Burns, A. T. Nelson, Microstructure dependent burst behavior of oxide dispersion–strengthened FeCrAl cladding, Materials & Design 234 (2023) 112307.
[30] M. Snead, Y. Yan, M. Howell, J. Keiser, K. Terrani, Severe accident test station design document, ORNL/TM-2015/556, Oak Ridge National Laboratory (2015).
[31] C. P. Massey, K. A. Terrani, S. N. Dryepondt, B. A. Pint, Cladding burst behavior of Fe-based alloys under LOCA, Journal of Nuclear Materials 470 (2016) 128–138.
[32] R. L. Williamson, J. D. Hales, S. R. Novascone, G. Pastore, K. A. Gamble, B. W. Spencer, W. Jiang, S. A. Pitts, A. Casagranda, D. Schwen, et al., BISON: A flexible code for advanced simulation of the performance of multiple nuclear fuel forms, Nuclear Technology 207 (7) (2021) 954–980.
[33] C. J. Permann, D. R. Gaston, D. Andrš, R. W. Carlsen, F. Kong, A. D. Lindsay, J. M. Miller, J. W. Peterson, A. E. Slaughter, R. H. Stogner, et al., MOOSE: Enabling massively parallel multiphysics simulation, SoftwareX 11 (2020) 100430.
[34] J. Hales, R. Williamson, S. Novascone, G. Pastore, B. Spencer, D. Stafford, K. Gamble, D. Perez, W. Liu, BISON theory manual the equations behind nuclear fuel analysis, Tech. rep., Idaho National Lab.(INL), Idaho Falls, ID (United States) (2016).
[35] P. Auerkari, Mechanical and physical properties of engineering alumina ceramics, no. 1792 in VTT Tiedotteita - Meddelanden - Research Notes, VTT Technical Research Centre of Finland, Finland, 1996.
[36] K. Kane, B. Garrison, S. Bell, B. Johnston, N. Capps, K. Linton, Report Summarizing Progress in Digital Image Correlation Analysis of Burst Phenomenon, Tech. rep., Oak Ridge National Laboratory (3 2022). doi:10.2172/1865738.
[37] C. B. Jensen, R. J. Armstrong, C. P. Folsom, N. E. Woolstenhulme, D. W. Kamerman, F. Cappia, D. M. Wachs, J. Harp, K. Linton, N. Capps, Combined TREAT-LOC & SATS Integral LOCA Experiment Plan, Tech. rep., Idaho National Laboratory (9 2022).
[38] A. K. Hoffman, R. V. Umretiya, V. K. Gupta, M. Larsen, C. Graff, C. Perlee, P. Brennan, R. Rebak, Oxidation Resistance in 1200°C Steam of a FeCrAl Alloy Fabricated by Three Metallurgical Processes, JOM. Journal of the Minerals, Metals & Materials Society 74 (4) (2 2022). doi:10.1007/s11837-022-05209-z.
[39] D. T. Hagrman, C. M. Allison, G. A. Berna, SCDAP/RELAP5/MOD 3.1 code manual: MATPRO, A library of materials properties for Light-Water-Reactor accident analysis. Volume 4 (6 1995). doi:10.2172/100327.
[40] K. J. Geelhood, C. E. Beyer, W. G. Luscher, PNNL stress/strain correlation for Zircaloy, Tech. rep., Pacific Northwest National Lab.(PNNL), Richland, WA (United States) (2008).
[41] M. Limbäck, T. Andersson, A Model for Analysis of the Effect of Final Annealing on the In- and Out-of-Reactor Creep Behavior of Zircaloy Cladding, in: Zirconium in the Nuclear Industry: Eleventh International Symposium, ASTM International, 1996. doi:10.1520/STP16185S.
[42] Y. Matsuo, Thermal Creep of Zircaloy-4 Cladding under Internal Pressure, Journal of Nuclear Science and Technology 24 (2) (1987) 111–119. doi:10.1080/18811248.1987.9735783.
[43] F. Erbacher, H. Neitzel, H. Rosinger, H. Schmidt, K. Wiehr, Burst criterion of Zircaloy fuel claddings in a loss-of-coolant accident, in: Zirconium in the Nuclear Industry, ASTM International, 1982.
[44] G. Pastore, S. R. Novascone, R. L. Williamson, J. D. Hales, B. W. Spencer, D. S. Stafford, Modelling of fuel behaviour during loss-of-coolant accidents using the BISON code, Proceedings of the TopFuel 2015 Conference (9 2015).
[45] A. Massih, Transformation kinetics of zirconium alloys under non-isothermal conditions, Journal of Nuclear Materials 384

(2009) 330–335.
[46] A. R. Massih, L. O. Jernkvist, Transformation kinetics of alloys under non-isothermal conditions, Modelling and Simulation in Materials Science and Engineering 17 (5) (2009) 055002.
[47] A. Massih, Evaluation of loss-of-coolant accident simulation tests with the fuel rod analysis code FRAPTRAN-1.4, Tech. Rep. TR11-008V1, Quantum Technologies AB (2011).
[48] G. Pastore, R. Williamson, R. Gardner, S. Novascone, J. Tompkins, K. Gamble, J. Hales, Analysis of fuel rod behavior during loss-of-coolant accidents using the bison code: Cladding modeling developments and simulation of separate-effects experiments, Journal of Nuclear Materials 543 (2021) 152537.
[49] H.-J. Neitzel, H. Rossinger, The development of a burst criterion for zircaloy fuel cladding under loca conditions, Tech. rep., Atomic Energy of Canada Ltd. (1980).
[50] V. Di Marcello, A. Schubert, J. van de Laar, P. Van Uffelen, The TRANSURANUS mechanical model for large strain analysis, Nuclear Engineering and Design 276 (2014) 19–29. doi:https://doi.org/10.1016/j.nucengdes.2014.04.041.

Declaration of Competing Interest

The authors declare that they have no known competing financial interests or personal relationships that could have appeared to influence the work reported in this paper.